

Laser machining of different diameter holes in alumina ceramic: Thermal stress analysis

B. S. Yilbas, S. S. Akhtar & C. Karatas

To cite this article: B. S. Yilbas, S. S. Akhtar & C. Karatas (2016) Laser machining of different diameter holes in alumina ceramic: Thermal stress analysis, Machining Science and Technology, 20:3, 349-367, DOI: [10.1080/10910344.2016.1191024](https://doi.org/10.1080/10910344.2016.1191024)

To link to this article: <https://doi.org/10.1080/10910344.2016.1191024>



Published online: 19 Jul 2016.



Submit your article to this journal [↗](#)



Article views: 224



View related articles [↗](#)



View Crossmark data [↗](#)



Citing articles: 2 View citing articles [↗](#)

Laser machining of different diameter holes in alumina ceramic: Thermal stress analysis

B. S. Yilbas^a, S. S. Akhtar^a, and C. Karatas^b

^aDepartment of Mechanical Engineering, King Fahd University of Petroleum and Minerals, Dhahran, Saudi Arabia; ^bEngineering College, Hacettepe University, Ankara, Turkey

ABSTRACT

Laser machining of different diameter holes into alumina tiles is carried out. Temperature and stress fields are predicted by using the finite element code. Surface temperature and residual stress predictions are validated through the thermocouple data and X-ray diffraction measurements. Morphological changes in the cutting section are examined by incorporating optical and scanning electron microscopes. It is found that the predictions of surface temperature and the residual stress formed at the cut section agree well with the experimental findings. In general, cut sections are free from large asperities; however, local dross attachments at the kerf edge and crack network formation at the kerf surface are observed.

KEYWORDS

Alumina; cutting; laser; stress; temperature

Introduction

Alumina tiles have good resistance to high temperature and wear. In the practical applications, net shaping of alumina tiles is difficult to achieve by using conventional machining methods because of their high hardness and brittle structures. Although net shaping through using fine alumina powders is possible, the process is expensive and, in most cases, results in pores in the final product. Laser machining offers considerable advantages over conventional methods, such as local treatment, nonmechanical contact between workpiece and machine tool, preciseness of operation, and fast processing. During laser processing, material undergoes solid heating and melting in the narrow region while generating high-temperature gradients in the machined section. This, in turn, causes high thermal stress levels in the laser-irradiated region and, in some cases, this limits the practical application of the parts machined, which is more pronounced when laser-machining the small parts. Moreover, thermal expansion of the machined parts depends on the thermal properties and the geometric features of the machined section, which influence thermal stress levels during machining. One of the examples of this kind is the circular cutting

CONTACT B. S. Yilbas  bsyilbas@kfupm.edu.sa  Department of Mechanical Engineering, King Fahd University of Petroleum and Minerals, KFUPM Box 1913, Dhahran 31261, Saudi Arabia.

Color versions of one or more of the figures in this article can be found online on at www.tandfonline.com/Imst.

© 2016 Taylor & Francis Group, LLC

of holes into alumina tiles where stress levels increase to the yielding limit of the substrate material. Consequently, comparative study for laser-cutting of holes into alumina tiles at different diameters becomes essential.

Considerable research studies were carried out to examine laser-cutting of ceramics. Nd:YAG laser-cutting of mullite-alumina was investigated by Pou et al. (2000). They demonstrated that the pulsed Nd:YAG laser connected to an optical fiber was a feasible and flexible tool for a successful cutting of mullite-alumina tiles. Fiber laser-cutting of thick-section alumina sheets was carried out by Yan et al. (2013). They showed that a transition from compressive to tensile stresses resulted in the workpiece as the laser-cutting parameters changed, which was found to be beneficial to resist crack formation during cutting. Femtosecond laser-cutting of alumina substrates was examined by Wang et al. (2010). They presented optimum laser-cutting conditions for quality cutting of alumina substrates and indicated the potential importance of laser applications in alumina-based electronic devices manufacturing. Simulation of laser-controlled thermal stress cutting of alumina ceramic was carried out by Cao et al. (2010). The findings revealed that as the laser power increased, the crack initiated earlier and the micro-crack of the fracture surface became large due to excessive tensile stress. Influence of machining parameters on surface roughness for laser micro-cutting of alumina–aluminum interpenetrating-phase composite was examined by Biswas et al. (2008). They indicated that Nd:YAG laser was capable of producing crack-free and smoothly cut edges. An active stress technique for laser-cutting of alumina was investigated by Akarapu and Segall (2006). They introduced probabilistic fracture mechanics approach to quantify the influence of the induced compressive stresses on the time and nature of the fracture during the cutting process. Formation of surface breaking in laser-cutting of alumina was examined by Tsai and Chen (2003). They incorporated a controlled fracture technique in the cutting process. The influence of glassy phase at the surface of alumina ceramics substrate on laser cutting was investigated by Renli et al. (2004). They demonstrated that the fast cooling of the liquid phase caused formation of extensive cracks network on the alumina surface, which degraded mechanical strength and thermal shock resistance of alumina substrate. Laser-controlled thermal stress cutting of an alumina ceramic was studied by Hu et al. (2011). They showed that the critical stress increased with increasing laser power and fracturing of the cut section became unavoidable for thinner workpieces. Surface finish and flexural characteristics of laser-cut alumina were examined by Shehata et al. (2007). They indicated that surface integrity of cut section improved significantly when hybrid laser/water jet cutting was used.

Laser-cutting holes and thermal stress fields in relation to end-product quality were studied earlier (Yilbas et al., 2011a, 2011b; 2012). The findings revealed that laser-cutting parameters, including cutting speed, laser output power, and the workpiece thickness, had significant effect on the end-product quality and the thermal stress fields developed in the cutting section. Although laser-cutting of alumina tiles and thermal stress analysis were carried out previously (Yilbas et al., 2013a; 2014), the size effect of the laser-cut holes into aluminum tiles was left for the future study.

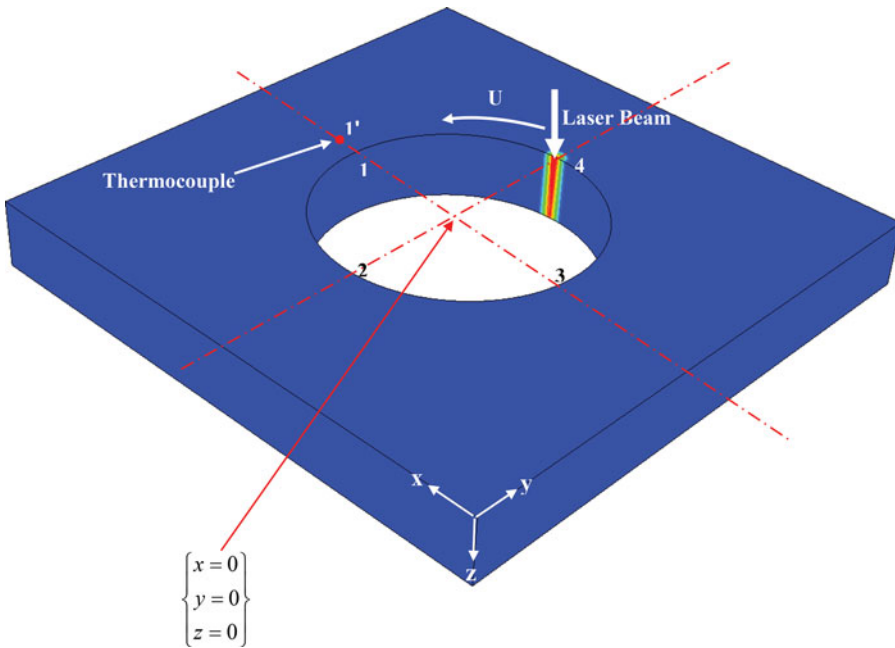


Figure 1. Schematic view of laser-cutting process and the location of thermocouple.

The size of the circular-cut geometry influences the thermal stress fields developed in the cutting section. Therefore, in the present study, laser-cutting of 10 and 15-mm diameter holes into 5-mm thick alumina tiles is introduced to assess the stress levels developed in the cut edges for different diameters. Morphological and metalurgical changes in the region of laser-cut sections are examined by using scanning electron microscopy (SEM), energy-dispersive spectroscopy, and X-ray diffraction (XRD). The residual stress predictions are compared with that obtained from the XRD technique.

Thermal stress analysis

Thermal analysis associated with cutting is given in the previous study (Yilbas et al., 2013b); therefore, only a brief description of the mathematical arrangements and numerical solutions are given herein. Figure 1 shows the schematic view of the laser circular cutting and the coordinate system.

The Fourier heat transfer equation pertinent to the laser heating process can be written as:

$$\rho \frac{DE}{Dt} = (\nabla(k\nabla T)) + S_o \quad (1)$$

where E is the energy gained by the substrate material, k is the thermal conductivity, and S_o is the heat source term resembling the laser beam, that is,

$$S_o = I_0 e^{-\delta z} (1 - r_f) e^{-\frac{(x-r\sin\omega t)^2 + (y-r\cos\omega t)^2}{a^2}} \quad (2)$$

I_o is laser power peak density, a is the Gaussian parameter, r_f is the surface reflectivity, ρ is the density, and x and y are the axes while the laser beam scans the surface along the circumference of the cut hole, then, $r = \sqrt{x^2 + y^2}$, that is, the circular cutting is carried out and the laser beam motion follows the circumference of the laser-cut hole with a constant angular velocity ω . The penetration depth of the laser beam after the key-hole formation is considered, that is:

$$\delta = \frac{1}{L} \ln \left(\frac{I_o}{I_L} \right) \quad (3)$$

where L is the thickness of the workpiece, I_o is the peak power intensity at the workpiece surface, and I_L is the laser power intensity at the workpiece thickness. The laser beam axis is parallel to the z -axis (Figure 1) and the laser beam intensity distribution is assumed to be Gaussian at the irradiated surface.

The convective and radiation boundary conditions are considered at the free surface of the workpiece. Therefore, the corresponding boundary condition is:

At the irradiated surface (top surface):

$$\frac{\partial T}{\partial z} = \frac{h_f}{k} (T_s - T_{amb}) + \frac{\varepsilon \sigma}{k} (T_s^4 - T_{amb}^4) \quad (4)$$

where $h_f [= 3,000 \text{ W/m}^2\text{K} \text{ (Yilbas et al., 1990)}]$ is the forced convection heat transfer coefficient due to the assisting gas.

At the bottom surface

$$\frac{\partial T}{\partial y} = \frac{h}{k} (T_s - T_{amb}) + \frac{\varepsilon \sigma}{k} (T_s^4 - T_{amb}^4) : \frac{\partial T}{\partial z} = \frac{h}{k} (T_s - T_{amb}) + \frac{\varepsilon \sigma}{k} (T_s^4 - T_{amb}^4) \quad (5)$$

where $h (= 20 \text{ W/m}^2\text{K})$ is the heat transfer coefficient due to natural convection, and T_s and T_{amb} are the surface and ambient temperatures, respectively, ε is the emissivity ($\varepsilon = 0.9$ is considered), σ is the Stefan-Boltzmann constant ($\sigma = 5.67 \times 10^{-8} \text{ W/m}^2\text{K}$). At far-away boundary (at the edges of the solution domain) constant temperature boundary is assumed ($T = 293 \text{ K}$), that is,

$$x = \infty; y = \infty; z = t_h \rightarrow T = 293K \quad (6)$$

where t_h is the thickness of the workpiece ($t_h = 0.003 \text{ m}$). Initially (prior to laser cutting), the substrate material is assumed to be at constant ambient temperature, that is, $T = T_{amb}$, which is considered as constant ($T_{amb} = 293 \text{ K}$).

Equation 1 is solved numerically with the appropriate boundary conditions to predict the temperature field in the substrate material. Table 1 gives the data used in the simulations in line with the experimental conditions. To incorporate the phase

Table 1. Simulation conditions.

L (m)	R (m)	I_o (W/m^2)	I_L (W/m^2)	ω (rad/s)
0.005	0.01 and 0.015	3.1×10^{12}	2.13×10^{12}	20

change, the enthalpy method is used (ABAQUS, 2014). The specific heat capacity is associated with the internal energy gain of the substrate material, that is,

$$C_p(T) = \frac{\partial U}{\partial T} \quad (7)$$

However, the internal energy gain during the phase change is associated with the latent heat of fusion, which is given separately in terms of solidus and liquidus temperatures (the lower and upper temperature bounds of the phase-change range) and the total internal energy associated with the phase change, called the latent heat (ABAQUS, 2014).

In the stress analysis, displacements are stored by ABAQUS at the nodal positions as a solution variable, and loads are defined as prescribed displacements and forces. Using the interpolation functions, it is possible to calculate the strain and stress increments at any point within the element using the compatibility and constitutive equations. ABAQUS transforms the mechanical equilibrium equations into a set of simultaneous equations, such that the nodal displacements and forces are related to each other through the elemental stiffness matrix. However, ABAQUS uses a temperature-dependent total thermal strain coefficient, $\alpha'(T)$. The differential and total thermal expansion coefficients are related to each other through:

$$\alpha'(T) = \frac{1}{T - T^o} \int_{T^o}^T \alpha(T) dT \quad (8)$$

where T^o is a reference temperature designating the point at which the material exhibits no dilatational strain (set to the mechanical coherency temperature in the current problem).

Laser heat flux with Gauss distribution and prescribed velocity of 15 cm/s along the X -axis through user subroutine DFLUX is applied to the thermal model. The Gaussian parameter “ a ” is $a = 0.000333$ m, in accordance with the experimental power intensity distribution, which was measured using the laser-output power meter. The thermal model consisted of two steps. The first step, which lasts 0.05 s, simulates the response of plate under moving laser heat flux. The second step, which lasts for 1,000 s, simulated the continued cooling in the model. Cooling was allowed to continue until all of the plate reaches initial temperature (room temperature). The temperature–time history resulted from the thermal analysis is used as input to the thermal stress analysis. The workpiece is considered as an elastic-plastic body, which is modeled as von Mises elastic-plastic material with isotropic hardening and with a yield stress that changes with temperature. In addition, a failure criterion based on damage strain is introduced. In this case, a simple empirical damage strain function, $\varepsilon_{\text{damage}}$, can be written as (Won et al., 1999):

$$\varepsilon_{\text{damage}} = \sum_{f_s=0.9}^{f_s=0.99} \Delta \varepsilon_{\text{flow}} \quad (9)$$

Table 2. Properties of alumina used in the simulations (Yilbas et al., 2013a).

T (K)	C_p (J/kg K)	k (W/m K)	E (Pa)	Poisson's ratio
300	786.19	37.06	3.80E + 11	0.270
400	939.53	28.19	3.75E + 11	0.272
500	1019.86	21.81	3.71E + 11	0.274
600	1071.45	17.23	3.66E + 11	0.276
700	1109.48	13.93	3.62E + 11	0.277
800	1140.27	11.56	3.57E + 11	0.279
900	1166.86	9.86	3.53E + 11	0.281
1,000	1190.84	8.63	3.48E + 11	0.283
1,100	1213.11	7.75	3.43E + 11	0.285
1,200	1234.22	7.12	3.39E + 11	0.287
1,300	1254.52	6.66	3.34E + 11	0.289

Cracks were expected to form when damage strain, $\varepsilon_{\text{damage}}$, exceeds the critical strain, ε_c :

$$\varepsilon_c = \frac{0.02821}{\varepsilon^{0.3131} \Delta T_B^{0.8638}} \quad (10)$$

where ΔT_B represents brittle temperature range below the melting temperature) (Li and Thomas, 2002). Tables 2 and 3 give the properties of alumina used in the simulations (Data Sheet, 2014).

In the sequential thermal-stress analysis, 142,468 elements are used while 132,140 hexahedral elements are used for the thermal-stress analysis. In addition, for the heat transfer analysis, mesh-used elements of type DC3D8 (8-node linear heat transfer brick) and stress analysis used C3D8 (8-node linear stress brick). Initially, the workpiece is considered to be free from stresses. In line with the experimental conditions, all the workpiece surfaces are set to be free from stresses, except the bottom edges of the workpiece, which are fixed, in which case, the workpiece is mounted at these locations on the x , y -table during the cutting process.

Experimental

The CO₂ laser (LC-ALPHAIII) delivering nominal output power of 2 kW was used to irradiate the workpiece surface. The nominal focal length of the lens used was 127 mm. The laser beam diameter focused at the workpiece surface will be about 0.3 mm. Nitrogen assisting gas emerging from the conical nozzle and co-axially with the laser beam was used. Laser-cutting experiments were repeated incorporating the different levels of laser-cutting parameters. The level of laser-cutting parameters resulting in the optimum cutting quality was selected. The cutting quality was judged by the minimum number of cracks at the cut surface and small-size dross

Table 3. Thermal expansion coefficient (α), solidus temperature (T_{solidus}), liquidus temperature (T_{liquidus}), and latent heat of melting (L_m) of alumina used in the simulations.

α (1/T)	T_{solidus} (K)	T_{liquidus} (K)	L_m (kJ/kg)
7.5×10^{-6}	2,260	2,323	900

Table 4. Laser heating conditions used in the experiment.

Scanning angle speed (rad/s)	Power (W)	Frequency (Hz)	Nozzle gap (mm)	Nozzle diameter (mm)	Focus setting (mm)	N_2 pressure (kPa)
20	2,000	500	1.5	1.5	127	600

attachments at the kerf edge. It should be noted that reducing scanning speed while increasing laser output power resulted in high rate of thermal erosion at the kerf inlet and formation of large cracks toward the kerf exit. However, reducing the scanning speed gave rise to a partially through cutting and large lateral cracks emanating from the cut edges. Laser treatment conditions are given in Table 4.

Alumina (Al_2O_3) tiles with 5-mm thickness were used as workpieces. Material characterization of the laser-nitrided surfaces was carried out using SEM and XRD. Jeol 6460 electron microscopy is used for SEM examinations and Bruker D8 Advanced having Cu-K α radiation is used for XRD analysis. A typical setting of XRD was 40 kV and 30 mA and scanning angle (2θ) was in the range of 20° – 80° . The position of the X-ray diffraction peak exhibits a shift as the specimen is rotated by an angle ψ . The magnitude of the shift is related to the magnitude of the residual stress. The relationship between the peak shift and the residual stress (σ) is given (Khana et al., 2005):

$$\sigma = \frac{E}{(1 + \nu)\sin^2\psi} \frac{(d_n - d_o)}{d_o} \quad (11)$$

where E is Young's modulus, ν is Poisson's ratio, ψ is the tilt angle, d_o is the stress free spacing, and d_n is the d spacing measured at each tilt angle. If there are no shear strains present in the specimen, the d spacing changes linearly with $\sin^2\psi$. The γ - Al_2O_3 peak takes place at 37.5° , which corresponds to (311) plane with the interplaner spacing of 1.23 Å. The linear dependence of $d(311)$ in Figure 2 results in the slope of -1.14×10^{-3} nm. The elastic modules and the Poisson's ratio of alumina are 380 GPa and 0.27, respectively. XRD measurements are repeated 3 times and the error related to the measurements is in the order of 3%.

To validate temperature predictions, a thermocouple was used to monitor the temporal variation of surface temperature at the location 0.5 mm away from the laser-cut edges to avoid the melting of the surface of the thermocouple during the laser-cutting process. The locations of the thermocouples are marked in Figure 1. The thermocouple output were calibrated according to the previous study (Shuja and Yilbas, 2000). The experimental error was determined using the experimental repeatability; therefore, the experiments were repeated 3 times and the error was estimated in the order of 5%.

Results and discussion

Laser-cutting of holes into 5-mm thick alumina tile is examined. Temperature and stress fields are predicted by using the ABAQUS finite element code in line with

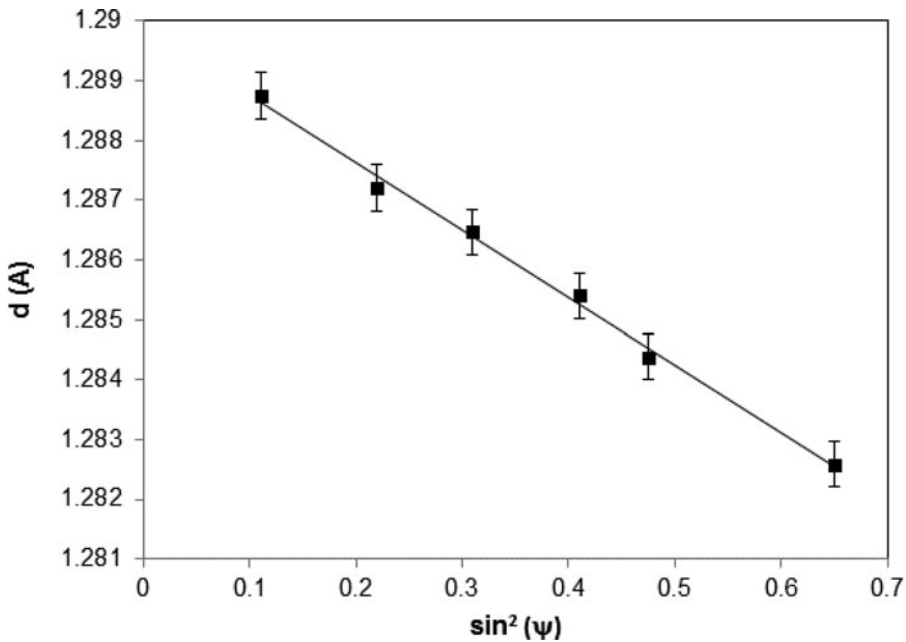


Figure 2. Linear dependence of $d(311)$ with $\sin^2\psi$.

the experimental conditions. Morphological and metallurgical changes in the cut section are analyzed by incorporating the analytical tools.

Figure 3 shows temporal variation of surface temperature predictions and the thermocouple data. It can be observed that both results are in good agreement and the small discrepancies between both findings are associated with the assumptions made in the simulations, such as isotropy, and the experimental error, which is in the order of 5%. Nevertheless, the differences are considerably small. To validate the predictions of the stress field, residual stress predicted is compared with the XRD measurements. The prediction of the residual stress in the surface region is in the order of -2.9 GPa, which is compressive and the measurement is -2.65 ± 0.08 GPa. Consequently, predictions agree well with the result of the XRD measurements.

Figure 4 shows temperature variation along the top and bottom circumferences of the holes for different cooling periods while Figure 5 shows temperature contours around the hole. Since the duration required for complete cutting of 10 and 15-mm diameter holes is different the cooling period starts at different time duration as shown in Figure 5. In addition, the maximum temperature attained for 10-mm diameter hole is about 2,825 K while it is about 2,738 K (Figure 5). This is associated with the heat dissipation around the hole circumference during cutting, which is slightly lower for the small-diameter hole than its counterpart for the large-diameter hole because of the total space where the heat conduction takes place around the hole circumference. Temperature reduces sharply around the hole circumference once the cooling period progresses. It should be noted that the cooling period initiates at different times for two hole diameters, in which case the cooling period starts at

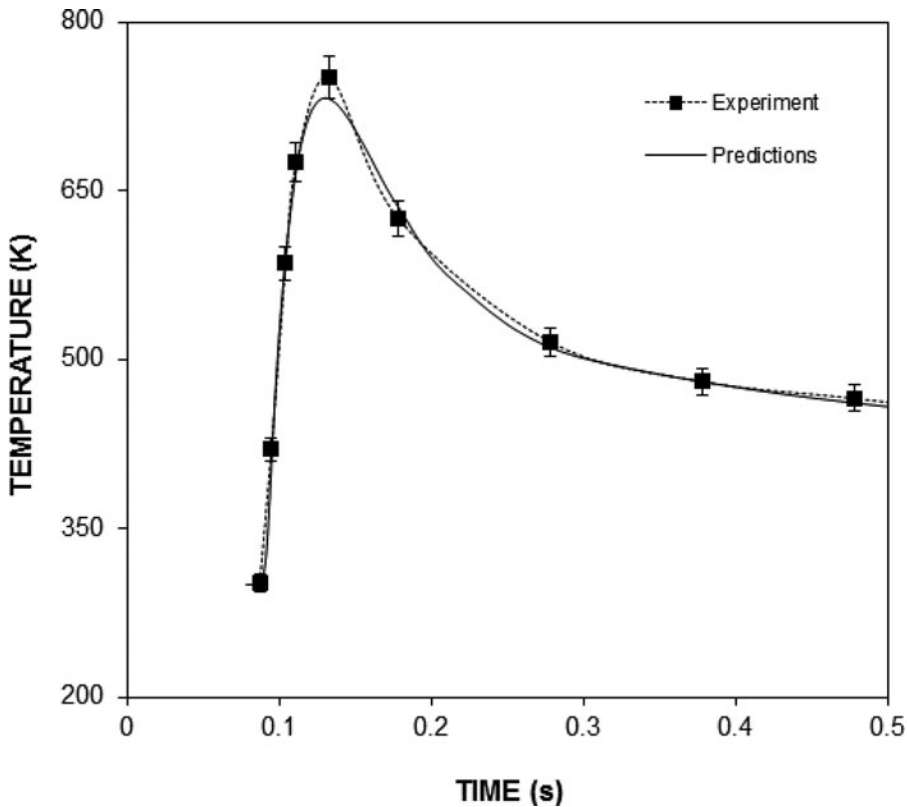


Figure 3. Temporal variation of surface temperature predicted from the simulations and obtained from thermocouple data.

$t = 0.21$ s for hole diameter of 10 mm and it is 0.314 s for the 15-mm hole diameter. Temperature decay from the melting temperature of the substrate material is at a higher rate for the 15-mm diameter hole than that corresponding to the 10-mm diameter hole. This is associated with the heat conduction taking place around the hole circumference. In this case, internal energy gain of the substrate material around the hole circumference causes temperature increase during the cutting process. Since the cutting speed is high enough, the rate of cooling is low due to conduction heat transfer from the hole's edges to solid bulk. This, in turn, results in high-temperature region remaining along the hole wall at the onset of cooling initiation. This behavior is true for top and bottom circumferences of the hole. In addition, temperature attains significantly high values at a location around the hole circumference where the laser beam is located and in the region in front of the laser beam temperature remains low prior to the start of the cooling cycle. This appears as a sharp decay of temperature as shown in Figure 4. Once the cooling cycle progresses further, temperature reduces significantly around the hole circumference. For both hole diameters. The convection, conduction, and radiation heat transfer from the hole wall is responsible for the rapid decay of temperature. Moreover, the presence of mushy zone due to phase change between the liquidus and solidus temperatures are evident from temperature curves. However, temperature increases above the

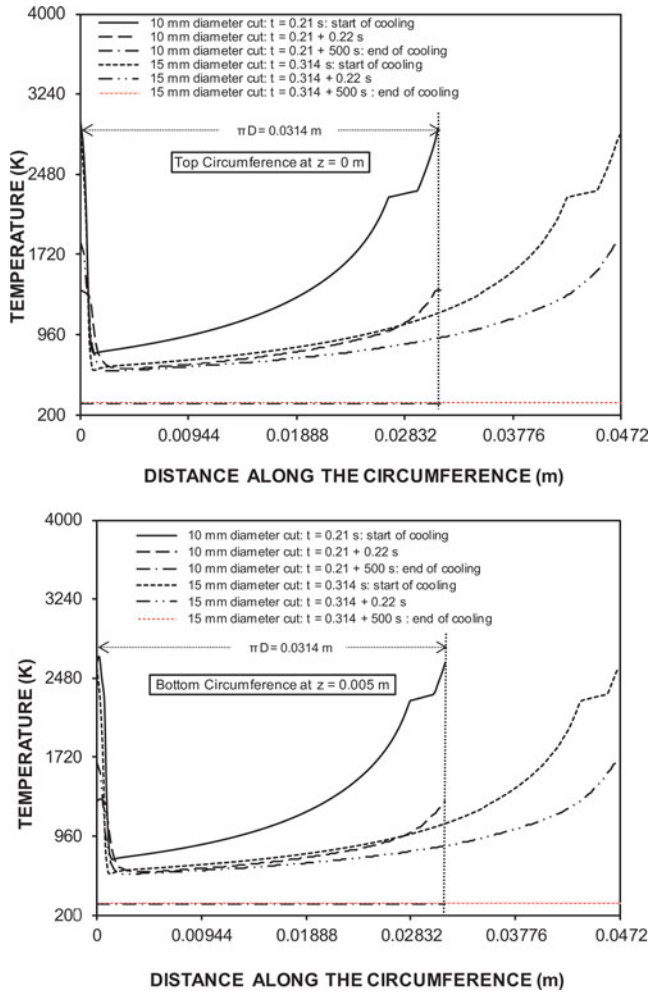


Figure 4. Temperature distribution along top and bottom circumferences of the hole for different cooling periods.

melting temperature of the substrate material in the central region of the irradiated spot, provided that temperature remains below the evaporation temperature of the substrate material. This causes superheating of the liquid phase in this region. This phenomenon disappears and replaces with solid-phase cooling once the cooling cycle progresses in this region. The maximum temperature is slightly lower at around the bottom circumference of the hole as compared to that corresponds to the top circumference. This is attributed to modelling of the absorption of the incident beam, which is governed with the Lambert's Beer law, in which case laser beam intensity reduces exponentially with reducing depth.

Figure 6 shows von Mises stress distribution along the top and bottom of the hole circumferences for different cooling periods while Figure 7 shows the contour plots of von Mises stress around the hole. von Mises stress remains low in the early cooling period when temperature is high. This is associated with the temperature-dependent elastic modulus of the substrate material. It should be noted that in the

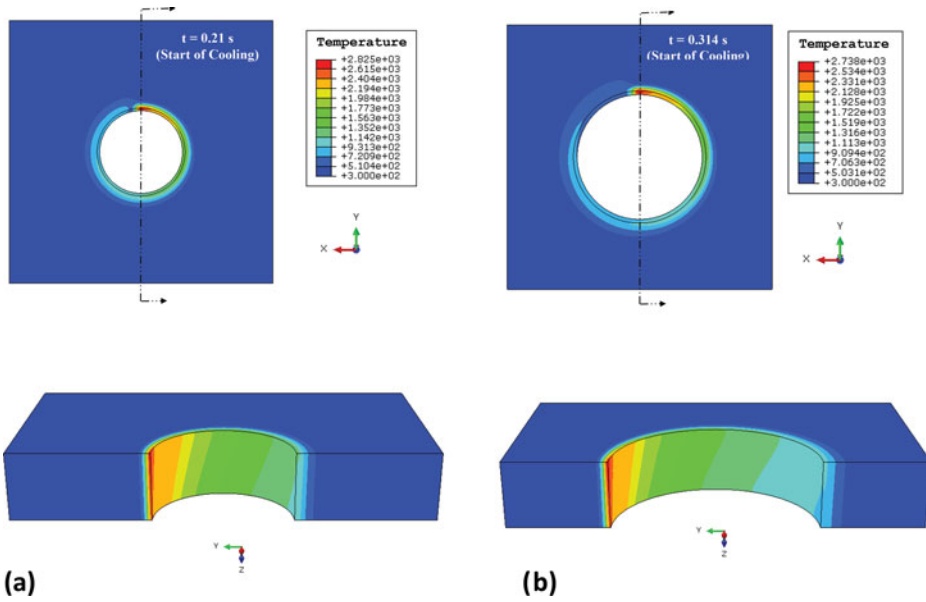


Figure 5. Temperature contours inside the workpiece for the two hole diameters: (a) 10 mm and (b) 15 mm.

simulations temperature-dependent elastic modulus is incorporated and as temperature increases, elastic modulus reduces. von Mises stress becomes small in the region where the cutting started at the end of the cooling periods. This is associated with the self-annealing effect of the lately cut sections. Heat transfer from the location of the laser beam toward the initially cut regions is responsible for low cooling rates around the initially cut region. This, in turn, generates self-annealing-effect while lowering the stress levels in this region. von Mises stress attains high values in the region where the temperature gradient is high. This corresponds to region in the vicinity of the irradiated spot when the cutting ceases off. When comparing von Mises stress distribution along the hole circumferences due to two different diameters, von Mises behaves almost the same for two diameters at the end of the cooling period. However, this behavior differs during the cooling period because of the differences in cooling rates for each hole diameter. This indicates that the stress levels developed around the hole circumference differ considerably during the cutting of each hole; however, this behavior changes once the cooling period ends after the cutting process. In this case, stress behavior and its magnitude becomes almost identical for both hole diameters. When comparing von Mises stress distribution around top and bottom circumferences, the magnitude of von Mises stress becomes lower at the bottom circumference as compared to top circumference. The difference between the stress distributions is associated with the cooling rates and temperature distribution at both circumferences, which differ slightly as observed from Figure 4.

Figure 8 shows temperature variation along the Z-axis for the two hole diameters and different cooling periods. It should be noted that $z = 0$ m represents the top surface and $z = 0.005$ m corresponds to the bottom surface of the hole. Temperature

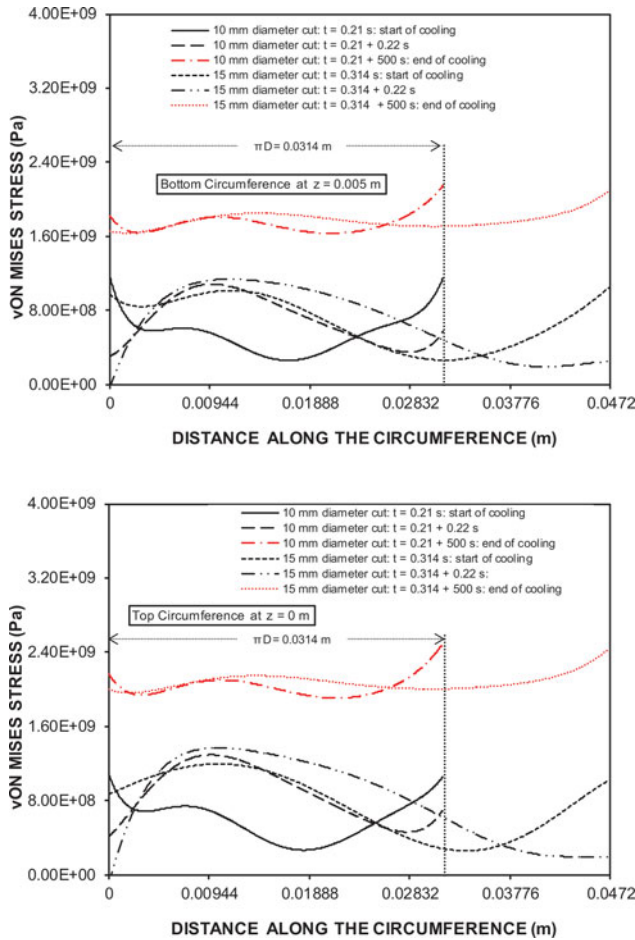


Figure 6. von Mises stress distribution along top and bottom circumferences of the hole for different cooling periods.

is slightly higher at the top surface than at the bottom surface. This is attributed to the absorption modelling of the incident radiation, in which case intensity decay is assumed to follow Lambert's Beer law along the z -axis. Temperature variation is almost linear along the z -axis and the temperature gradient is low. Temperature decays rapidly as the cooling period progresses, which is true for both diameters of the hole. **Figure 9** shows von Mises stress along the z -axis for two hole diameters and different cooling periods. von Mises stress attains lower values in the region close to the top and bottom surfaces of the hole. This is attributed to free expansion of the surfaces. In this case, surface thermally expands freely at the surface, since there is no constraint present at the surface. This lowers the strain and stress levels in this region. This situation changes in the region of the mid-thickness of the work-piece. In this case, von Mises stress attains high values because of the high strain formed in this region. The heated material is not free to expand in this region and the high strain formed is due to the high-temperature heating during the cutting in this region. The maximum value of von Mises stress is in the order of 3.5 GPa,

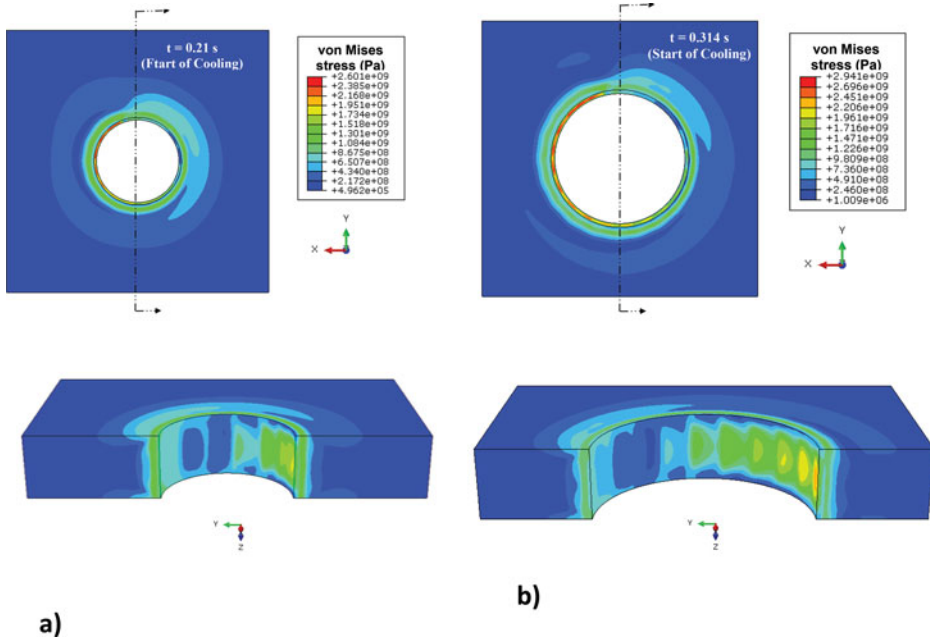


Figure 7. von Mises stress contours inside the workpiece for the two hole diameters: (a) 10 mm and (b) 15 mm.

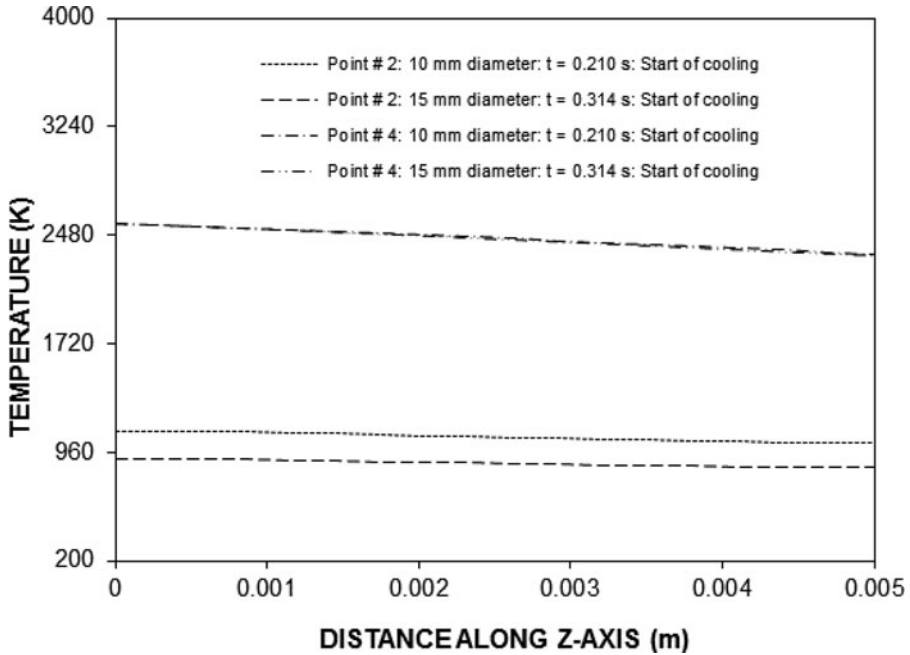


Figure 8. Temperature distribution along the z-axis at the onset of cooling starts for two locations along the hole circumference (Figure 1). $z = 0$ m corresponds to the hole's top surface and $z = 0.005$ m is the hole's bottom surface.

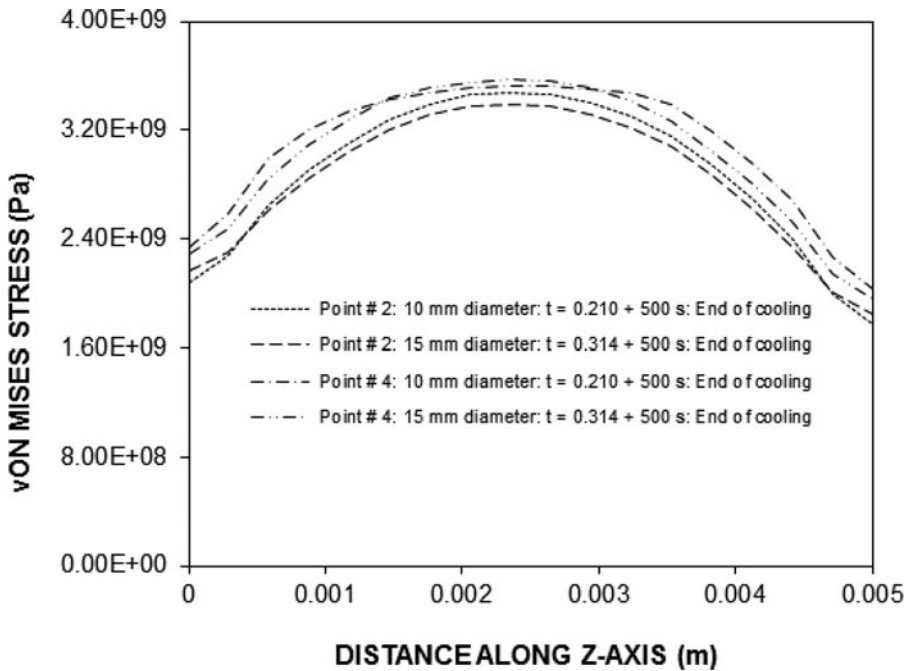


Figure 9. von Mises stress distributions along the z-axis at the end of the cooling periods for two locations along the hole circumference (Figure 1). $z = 0$ m corresponds to the hole top's surface and $z = 0.005$ m is the hole's bottom surface.

which is considerably high as compared to that predicted for metals (Krishnan et al., 2001). The influence of hole diameter on von Mises stress is not considerable, provided that von Mises corresponding to the 10-mm diameter is slightly higher than that of 15-mm diameter.

Figure 10 shows SEM micrographs of laser-cut section. It is evident from the micrographs that the cut edges are free from large defect sides and no major cracks are observed. Unlike metals (Yilbas and Arif, 2011), the sideways burnings around the cut edges are not visible. The striation pattern is evident from the SEM micrographs. The formation of striations is because of instabilities associated with the melt flow at the kerf surface during the cutting. However, the depth of the striations is shallow due to the low thermal conductivity of aluminum, in which case thermal erosion caused by the heat diffusion is not substantial as it is the case for metals (Krishnan et al., 2001). The striations are slightly bent toward the kerf exit and are closely spaced. This behavior is attributed to the change in the viscosity of the molten flow that decreases due to the reduction in temperature at the kerf exit region. Although high-pressure assisting gas is used to purge the molten flow out of the kerf width during the cutting, the shear force developed in the molten flow increases significantly due to the high flow. This, in turn, modifies the flow pattern toward the kerf exit and striation patterns changes in this region. In addition, the momentum of the assisting gas reduces toward the kerf exit, which in turn results in reduced drag force in this region. The dross attachment at the kerf exit is evident from the SEM micrograph. This occurs because of the attainment of relatively

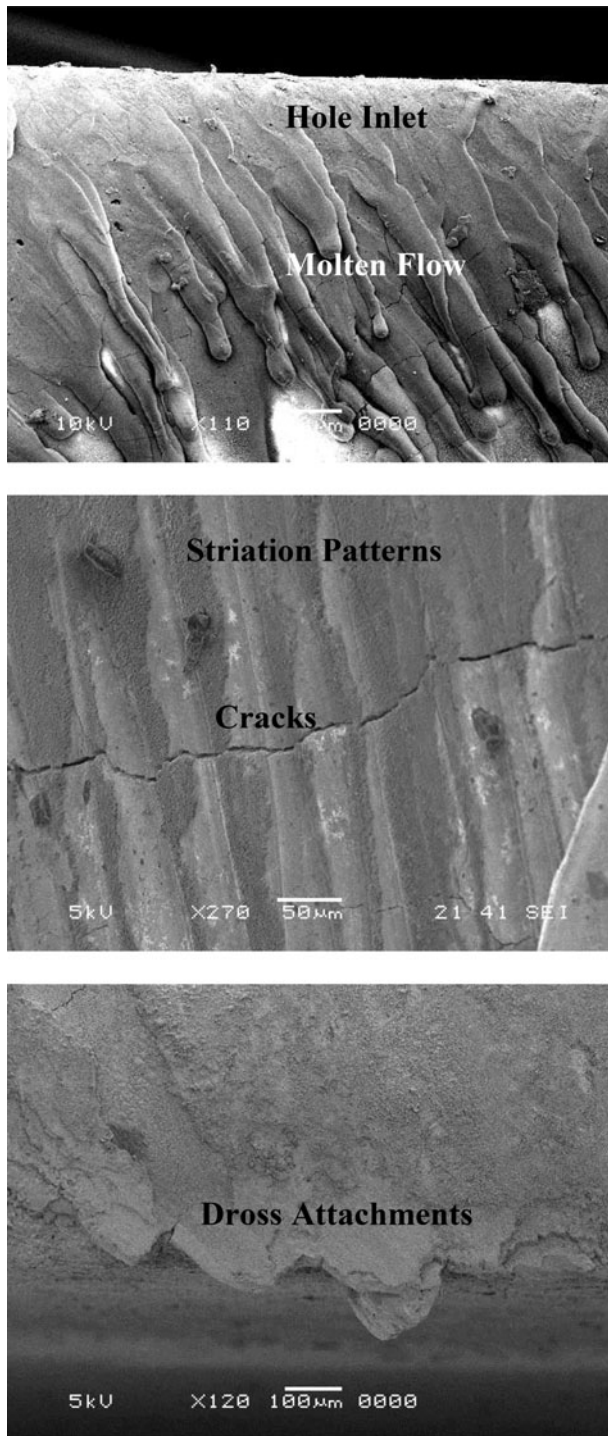


Figure 10. SEM micrographs of the laser-cut hole surfaces. *Note:* SEM, scanning electron microscopy.

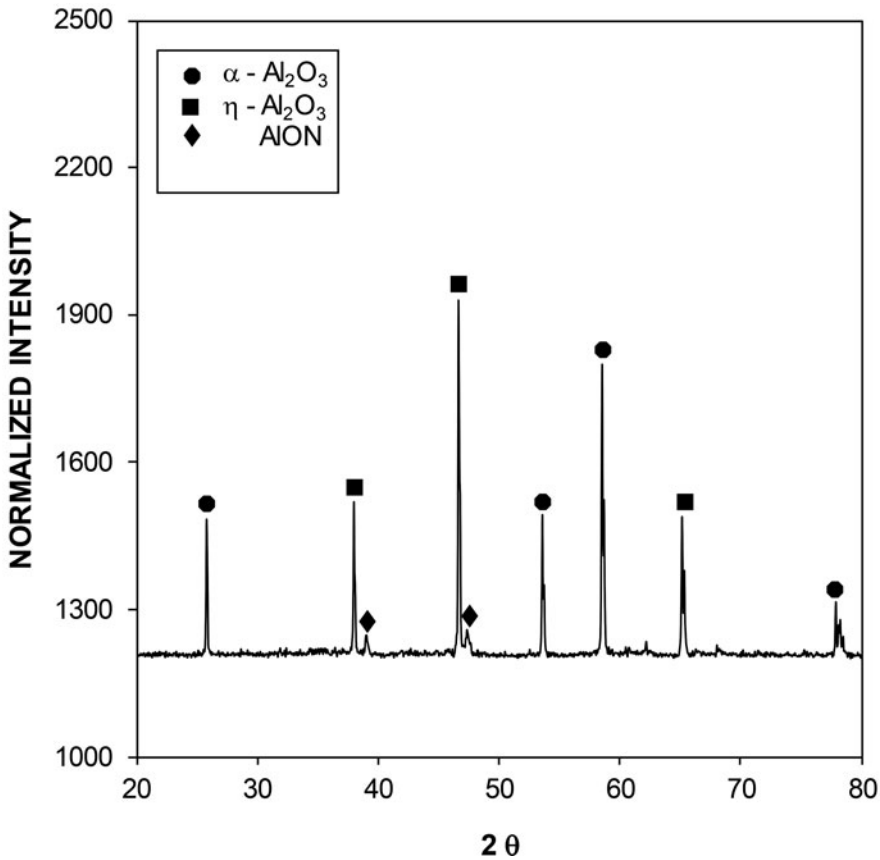


Figure 11. X-ray diffractogram for the laser-cut section.

low temperature (slightly above the liquidus temperature) at the circumference of the hole's exit because of the convection cooling of the assisting gas. The reduced temperature increases the viscosity of the molten flow at the kerf exit. In addition, assisting gas reduces its axial momentum due to the flow friction in the narrow kerf width. Consequently, combination of high-viscosity molten and low assisting-gas pressure reduces the rate of molten material ejected from the kerf exit. The remaining molten material, which is not ejected from the kerf exit, attaches the kerf while forming the burrs at the hole exit. The cracks are formed at the kerf surface, which is associated with the high cooling rates. It should be noted that high cooling rates results in the formation of brittle and dense structures at the surface in the form of re-cast layer. The fracture toughness of this layer becomes significantly lower than the as-received material fracture toughness (Yilbas et al., 2009). Consequently, high residual stress formation in the re-cast layer causes the crack formation in this layer. However, the close examination of the SEM micrographs indicates that the cracks formed at the kerf surface are shallow and do not extend below the re-cast layer thickness. This can be attributed to the stress relaxation in this region. It should be noted that energy relaxation takes place through cracking in this region.

Figure 11 shows XRD diffractogram for the laser-cut surface. The presence of stable α - Al_2O_3 peak in the diffractogram reveals the transformation of γ - Al_2O_3 into a stable α - Al_2O_3 at high temperature. It should be noted that α - Al_2O_3 and γ - Al_2O_3 are in accordance with ICDD 46–1212 card and ICDD 25–1133 card, respectively. The formation of thermodynamically stable α - Al_2O_3 phase can be attributed to thermal relaxation of nonequilibrium γ - Al_2O_3 phase that has a defective spiral structure (Damani and Makroczy, 2000). In addition, the use of nitrogen at high pressure causes the formation of ALON compound at the kerf surface and ALON formation contributes to the brittleness of the re-cast layer formed at the kerf surface.

Conclusion

Laser hole cutting into alumina tiles is carried out and the effect of hole diameters on temperature and stress fields are analyzed. ABAQUS finite element code is used to predict thermal stress fields. Surface temperature and residual stress predictions are validated thorough the thermocouple data and XRD measurements. Morphological changes in the cutting section are examined by incorporating the analytical tools. It is found that temperature decay is sharp around the hole circumference for 15-mm-diameter hole as compared to that of 10-mm-diameter hole. This behavior is attributed to the internal energy gain of the substrate material in the region of the hole circumference and heat transfer losses from this region to the solid bulk. Von Mises stress shows similar behavior around hole circumference for both hole diameters. Heat conduction from the region where laser spot is last located to the location where cutting is started causes self-annealing effect in the region where the initial cutting commenced. This in turn results in low stress levels in this region at the end of the cooling period. The residual stress predicted is compressive and it is in the order of -2.9 GPa and the residual stress measured using the XRD technique is in the order of -2.65 ± 0.08 GPa. Consequently, both results appear to be in very good agreement. In addition, surface temperature predicted agrees well with the thermocouple data. The morphological examination of the cut sections reveals that striation patterns are formed at the kerf surface, provided that the stria depth is shallow. Temperature drop toward the kerf exit causes the increase in the viscosity of the molten flow in this region. The pressure drop due to friction effect in the narrow kerf depth lowers the pressure drag of the assisting gas acting on the molten flow. These in turn reduce the molten ejection from the kerf and formation of dross attachments at the kerf exit. High cooling rates at the kerf surface causes the formation of brittle re-cast layer, which endures multi-micro cracking, provided that cracks are shallow and do not extend into the substrate material.

Acknowledgments

The authors acknowledge the support of King Fahd University of Petroleum and Minerals, Dhahran, Saudi Arabia for this work.

References

- ABAQUS Theory Manual, Version 6.2, ABAQUS Inc., Pawtucket, USA, 2014.
- Akarapu, R.; Segall, A. E. (2006) Numerical simulations of an active-stressing technique for delaying fracture during cutting of alumina. *Journal of Manufacturing Science and Engineering, Transactions of the ASME*, 128(4): 921–927.
- Biswas, R.; Kumar, A. S.; Mitra, S. (2008) Influence of machining parameters on surface roughness in Nd:YAG laser micro-cutting of alumina-aluminium interpenetrating phase composite. *International Journal of Surface Science and Engineering*, 2(3–4): 252–264.
- Cao, Q.; Hu, J.; Luo, J. (2010) Simulation and analysis of laser-controlled thermal stress cutting of alumina ceramic. *Chinese Journal of Lasers*, 37: 345–349.
- Damani, R. J.; Makroczy, P. (2000) Heat treatment induced phase and microstructural development in bulk plasma sprayed alumina. *Journal of the European Ceramic Society*, 20: 867–888.
- Data Sheet. (2014). Available: www.vtt.fi/inf/pdf/tiedotteet/1996/T1792.pdf.
- Hu, J.; Cao, Q.-Q.; Luo, J.-W. (2011) Numerical analysis of laser-controlled thermal stress cutting of an alumina ceramic. *Lasers in Engineering*, 21: 47–61.
- Khana, Z. A.; Hadfield, M.; Tobe, S.; Wang, Y. (2005) Ceramic rolling elements with ring crack defects—a residual stress approach. *Materials Science and Engineering A*, 404: 221–226.
- Krishnan, R.; Dash, S.; Rao, C. B.; Rao, R. V. S.; Tyagi, A. K.; Raj, B. (2001) Laser induced structural and microstructural transformations of plasma sprayed Al₂O₃ coatings. *Scripta Materialia*, 45: 693–700.
- Li, C.; Thomas, B. G. (2002) Thermo-mechanical finite element model of shell behavior in the continuous casting of steel. *Sixth Asia-Pacific Symposium on Engineering Plasticity and Its Applications*, Sydney, NSW, Australia, 2nd–6th December 2002, Trans. Tech., 827–834.
- Pou, J.; Quintero, F.; Lusquinos, F.; Larosi, M.; Soto, R.; Perez-Amor, M. (2000) Nd:YAG laser cutting of mullite-alumina. *Proceedings of the Laser Materials Processing Conference. ICALEO'99. LIA*. San Diego, USA, 2000, 87, C166–75.
- Renli, F.; Yanbo, L.; Xin, X.; Ferreira, J. M. F. (2004) Characterization of glassy phase at the surface of alumina ceramics substrate and its effect on laser cutting. *Materials Science Forum*, 455–456: 322–325.
- Shehata, G.; Molian, P.; Bastawros, A.; Shrotriya, P. (2007) Surface finish and flexural strength of CO₂ laser-cut alumina by evaporative and thermal stress fracture modes. *Transactions of the North American Manufacturing Research Institute of SME*, 35: 391–399.
- Shuja, S. Z.; Yilbas, B. S. (2000) The influence of gas jet velocity in laser heating—a moving work-piece case. *Proceedings of the Institution of Mechanical Engineers, Part C: Journal Mechanical Engineering Science*, 214: 1059–1078.
- Tsai, C.-H.; Chen, C.-J. (2003) Formation of the breaking surface of alumina in laser cutting with a controlled fracture technique. *Proceedings of the Institution of Mechanical Engineers, Part-B: Journal of Engineering Manufacture*, 217(4): 489–497.
- Wang, X. C.; Zheng, H. Y.; Chu, P. L.; Tan, J. L.; Teh, K. M.; Liu, T.; Ang, B. C. Y.; Tay, G. H. (2010) High quality femtosecond laser cutting of alumina substrates. *Optics and Lasers in Engineering*, 48: 657–663.
- Won, Y.; Yeo, T.-J.; Seol, D.; Oh, K. (1999) A new criterion for internal crack formation in continuously cast steels. *Metallurgical and Materials Transactions*, 31B(4): 779–794.
- Yan, Y.; Ji, L.; Bao, Y.; Chen, X.; Jiang, Y. (2013) CO₂ laser high-speed crack-free cutting of thick-section alumina based on close-piercing lapping technique. *The International Journal of Advanced Manufacturing Technology*, 64(9): 1611–1624.
- Yilbas, B. S.; Akhtar, S. S.; Chatwin, C. (2011a) Laser hole cutting into bronze: Thermal stress analysis. *Optics and Laser Technology*, 43(7): 1119–1127.

- Yilbas, B. S.; Akhtar, S. S.; Karatas, C. (2011b) Laser trepanning of a small diameter hole in titanium alloy: Temperature and stress fields. *Journal of Materials Processing Technology*, 211(7): 1296–1304.
- Yilbas, B. S.; Akhtar, S. S.; Karatas, C. (2012) Laser hole cutting into Ti-6Al-4V alloy and thermal stress analysis. *International Journal of Advanced Manufacturing Technology*, 59(9–12): 997–1008.
- Yilbas, B. S.; Akhtar, S. S.; Karatas, C. (2013a) Laser cutting of alumina tiles: Heating and stress analysis. *Journal of Manufacturing Processes*, 15(1): 14–24.
- Yilbas, B. S.; Akhtar, S. S.; Karatas, C. (2014) Laser cutting of triangular geometry into alumina tiles: Morphological changes and thermal stress analysis. *Machining Science and Technology: An International Journal*, 18(3): 424–447.
- Yilbas, B. S.; Akhtar, S. S.; Keles, O. (2013b) Laser cutting of triangular geometries in aluminum foam: Effect of cut size on thermal stress levels. *Optics and Laser Technology*, 48: 523–529.
- Yilbas, B. S.; Arif, A.F. M. (2011) Laser cutting of steel and thermal stress development. *Optics and Laser Technology*, 43: 830–837.
- Yilbas, B. S.; Davies, R.; Gorur, A.; Yilbas, Z.; Begh, F.; Kalkat, M.; Akcakoyun, N. (1990) Study into the measurement and prediction of penetration time during CO₂ laser cutting process. *Proceedings of the Institution of Mechanical Engineers, Part B, Journal of Engineering Manufacture*, 204: 105–113.
- Yilbas, B. S.; Karatas, C.; Arif, A. F. M.; Aleem, B. J. A. (2009) Laser gas assisted nitriding of alumina surfaces. *Surface Engineering*, 25(3): 235–240.